Arabian Journal of Chemistry (2023) **16**, 105112

King Saud University

Arabian Journal of Chemistry

www.ksu.edu.sa
www.sciencedirect.com

ORIGINAL ARTICLE

Investigating the effect of milling time on structural, mechanical and tribological properties of a nanostructured hiped alpha alumina for biomaterial applications

Mamoun Fellah [a,b], Naouel Hezil [c], Dikra Bouras [d], Alex Montagne [e], Aleksei Obrosov [f], Wasim Jamshed [g,*], Rabha W. Ibrahim [h,i,j], Amjad Iqbal [k,l], Sayed M El Din [m], Hamiden Abd El-Wahed Khalifa [n,o]

[a] *Mechanical Engineering Department, ABBES Laghrour-University, Khenchela, P.O 1252 40004, Algeria*
[b] *Tribology and Materials Group, Laboratory of Foundry, Badji Mokhtar University, Annaba, B. O, 12 CP 23000. Algeria*
[c] *Mater Sciences Department, ABBES Laghrour – University, Khenchela P.O 1252, 40004, Algeria*
[d] *Laboratoryof Active Components and Materials, Larbi Ben M'Hidi University, Oum El Bouaghi 04000, Algeria*
[e] *Mechanical Engineering Department, King Fahd University of Petroleum and Minerals. Box 1180, Dhahran 31261, Saudi Arabia*
[f] *Department of Physical Metallurgy and Materials Technology, Brandenburg Technical University, Konrad-Wachsmann Allee 17, 03046 Cottbus, Germany*
[g] *Department of Mathematics, Capital University of Science and Technology (CUST), Islamabad 44000, Pakistan*
[h] *Department of Computer Science and Mathematics, Lebanese American University, 13-5053 Beirut, Lebanon*
[i] *Near East University, Mathematics Research Center, Department of Mathematics, Near East Boulevard, PC:99138, Nicosia, / Mersin 10, Turkey*
[j] *Information and Communication Technology Research Group, Scientific Research Center, Al-Ayen University, Thi-Qar, Iraq*
[k] *Department of Materials Technologies, Faculty of Materials Engineering, Silesian University of Technology, 44-100 Gliwice, Poland*
[l] *CEMMPRE—Centre for Mechanical Engineering Materials and Processes, Department of Mechanical Engineering, University of Coimbra, Rua Lu's Reis Santos, 3030-788 Coimbra, Portugal*
[m] *Center of Research, Faculty of Engineering, Future University in Egypt New Cairo 11835, Egypt*
[n] *Department of Mathematics, College of Science and Arts, Qassim University, Al-Badaya 51951, Saudi Arabia*
[o] *Department of Operations and Management Reseatch, Faculty of Graduate Studies for Statistical Research, Cairo University, Giza 12613, Egypt*

Received 24 March 2023; accepted 23 June 2023
Available online 28 June 2023

* Corresponding author.
E-mail address: wasiktk@hotmail.com (W. Jamshed).

Peer review under responsibility of King Saud University. Production and hosting by Elsevier.

Production and hosting by Elsevier

https://doi.org/10.1016/j.arabjc.2023.105112

KEYWORDS

α-Al_2O_3;
Milling time;
Nanomaterials;
Particle size;
Hardness;
Biomaterials;
Biomedical applications

Abstract In this work was prepared α-Al_2O_3 alloys from laboratory aluminum oxide powder that was milled for different periods of time and sintered at a temperature of 1450 °C. The difference between the prepared samples was studied using several experimental measurement techniques, including X-ray diffraction, scanning electron microscopy and measurement of physical and mechanical properties. Moreover, the effect of milling time on the formation and sintering of alpha-alumina, by milling the mixture at different times using high energy crushing technique was studied. An influence of milling time on density, open spaces and microstructure of the samples was analyzed. The obtained results showed that longer milling duration led to alloys with higher hardness (H) and modulus of elasticity (E). This improvement is due to lower porosity and corresponding higher density at high temperatures. A noticeable decrease in the size of the particles with the increase of the milling time led to an increase in the lattice parameter accompanied by a decrease in defects and ionic voids. The percentage of pores reached 0.04 % within 24 h of grinding after it was approximately 0.20 %, while the density reached 96 % after the same highest grinding time. Tests showed that the value of friction coefficient decreases, while it increases with the increase in the applied pressure force and this was confirmed by SEM images of the samples. the main factor to reduce friction is the increase in grinding time, regardless of the value of the applied load. The results showed that the Al_2O_3 alloy applied to it with a load of 2 N and milled for 24 h had a minimum value of 1.94 μm^3 wear volumes and a wear rate of 1.33 ($\mu m^3 \cdot N^{-1} \cdot \mu m^{-1}$). The sample milled for 24 h showed the best result, characterized by the lowest wear size, specific wear rate and the highest hardness with extraordinary density of 96 %, which is important in the field of biomaterials applications.

1. Introduction

Many researchers (Nina Zamosteanu Filip, 2022; Marin et al., 2020) have discussed the issues with friction and wear in knee and hip replacement prostheses because of how critical they are to the functionality of these types of prostheses. Components for the head and cup are chosen by taking into account a variety of characteristics, including biocompatibility, durability against corrosion and durability against mechanical friction, and wear. Following then, ceramic items have been successfully employed in total arthroplasty of the hip in Europe (Ramakrishna et al., 2001; Ghasemi-Mobarakeh et al., 2019). In comparison to alloys of metal, these kinds of elements offer a variety of potential advantages. Both research using animals and human trials in Europe have demonstrated their good biocompatibility (Bhaskar and Biomaterials, 2021). An extremely strong resistant to scratching polish can be applied to porcelain. Low friction explanations with outstanding wear attributes are made possible by that property, which works in conjunction with the material's water absorption and durability against corrosion. Given that these unprocessed components are malleable and can be readily acquired because they are abundant, evidence from history demonstrates that man employed clay materials and clay to form some of the materials he would have required throughout all phases of his life in the past (Fellah et al., 2019; Li et al., 2022; Valiev et al., 2020). In contrast, ceramic materials (González-Masís et al., 2021), contrary to substances and organic materials, have a combination of incredible chemical and physical attributes that competent them to be employed in the traditional (Wang et al., 2021). From it, scientific research has recently tended to search for new vital materials in order to use it in various fields (Mechanical, 2019). One of the most important of these materials is bioceramics, which are bioactive industrial materials and are used in the medical field, as well as in the biological system of the living organism, as if they are biocompatible with the body and are able to create links between them and the living tissue (Bouras et al., 2018; Bouras et al., 2020).

Since elements were being used at the beginning of the 19th century for various purposes, processes caused by metals were researched. Animal studies on gold, silver, lead, nickel, and platinum revealed that platinum had a favorable response (Bouras et al., 2021). Other metals, such as silver, platinum, lead, and aluminum, caused rapid corrosion, tissue discolouration, and lacked acceptable physical properties. In light of their biocompatibility and advantageous mechanical qualities, CoCrMo alloys, titanium, and the alloys thereof were then suggested as attractive possibilities for medical uses. The present NC pure titanium (Ti) and its alloys, NC SMAs, NC SS, and NC biodegradable aluminum alloys including Fe- and Mg-based alloys are all examples of nanostructured (NC) metallic compounds (Bouras et al., 2021; Dai et al., 2020; Venkatraman and Choudhary, 2022; Hamisah Ismail, 2021). The metallic alloys with nanostructures open up fresh possibilities and ideas for surgical implants, benefiting technology for medical devices in all its forms. According to data from multiple research, nanostructured metallic biomaterials exhibit enhanced physical and mechanical capabilities following NC processing, making them appealing (Bouras et al., 2021; Dai et al., 2020; Venkatraman and Choudhary, 2022; Hamisah Ismail, 2021).

Aluminum oxide is one of the most important and most widely used vital materials in the field of bone replacement in the body (Singh et al., 2022; Tang and Yuxi, 2015; José Hafid Roque-Ruiz, 2019; Rodriguez Olguin et al., 2022; Li et al., 2019; Kim et al., 2018; Krause et al., 2020), as it is a bioactive material and has the ability to form a good adhesion layer that connects it with living tissue, and this does not have any side effects on the body, unlike mineral materials that are it is corrosive and does not bind with the living medium (Jalili et al., 2020). Although alumina has strong mechanical properties when sintering at high temperatures that made it widely used, it has some shortcomings, and this prompted researchers to find solutions to improve its mechanical properties more and make it close and more suitable for use in human bone compounds, and among the most important of this solution is to introduce some additions to it (El-Kheshen et al., 2008; Tripathi et al., 2015).

For several decades, all forms of prostheses, biomaterials and different operating procedures were tried. Nevertheless, these techniques, based more on empirical techniques than rigorous scientific protocols, usually resulted in unsatisfactory results with, in the majority of cases, the lifespan of the implants, limited to an average of 10–20 years, which remains a major problem (Pietrzyk et al., 2020). This study is dedicated to understanding the mechanisms of degradation of total hip prostheses (THAs) (Suárez et al., 2021), which aim to replace the coxo-femoral joint destroyed following a lesion at the hip level, or an accident such as rupture femoral neck, etc. The number of PTH poses is increasing under the dual effect of the aging of the population and the implantation of PTH in increasingly young patients to limit surgical reoperations, so it is important to increase the lifespan PTHs (Granchi, 2017; Gallart et al., 2018), which is the great concern of the science of biomaterials which aspires to regularly develop new materials that are more resistant, harder, more chemically stable and of better biocompatibility (Jing et al., April 2022; Rolfson et al., 2016).

Biomaterials currently in use include metals, polymers and ceramics, such as alumina (Fellah et al., 2019; Roualdes et al., 2010). Thanks to their very good resistance to wear and their good mechanical behavior, ceramics are widely used to manufacture femoral heads and acetabular cups, they are bioinert and have very good biocompatibility. One of the most frequent problems after the implantation of a hip prosthesis is the production of wear debris. This debris disrupts cellular metabolism, ultimately, bone resorption occurs, leading to aseptic loosening of the prosthesis. Thanks to their hardness, this problem is less common with ceramics than with other biomaterials such as very high molecular weight polyethylene (UHMWPE) or metal alloys. Ceramics are brittle and can fracture when subjected to impact damage (Anjaneyulu et al., 2019). In this way, it is easier to understand the degradation mechanisms of materials, which makes it possible to improve them.

Manufacturing nanomaterials in an easy, affordable, and high-yield method has been a significant challenge since the inception of nanoscience. Numerous bottom-up and top-down approaches have been developed for the commercial production of nanotubes. Widely employed in the creation of various nanomaterials, nanograins, nanoalloys, and nanocomposites is high-energy dry ball milling. Adnan Abu-Surrah & Yahya Al-Degs have also enhanced the physical grinding of inorganic solid waste into nanosize (1–100 nm) (Abu-Surrah and Al-Degs, 2022).

The high-energy milling technology is a preparation process for the production of new materials that causes the powders to break down and recombine between the particles formed, and this technology eventually leads to an atomic mixture between the atoms of the starting elements as the high energy milling is stabilized in the equilibrium stages, and is used as a means to activate certain reactions or to form new phases, due to the energy that is introduced during milling (Abu-Surrah and Al-Degs, 2022; Fellah et al., 2017).

Milling time is one of the main factors that control the dimensions and morphology of the final powder. Where the determination of the optimal crushing time, specific for each compound and variable according to the crushing conditions, requires follow-up by structural morphological characterizations and specific milled times (Fellah et al., 2020). Whether it is for forming alloys, composites or others, it is necessary to go through this experimental process to obtain the desired compound (Zhang, 2004).

In this work is prepared and develop ceramic materials consisting mainly of commercial aluminum oxide powder, where these mixtures was mixed at different times using high energy crushing technology. One of the most important goals we set for the -Al2O3 alloy in the present research is to find out an association between the process of s temperature, microstructure, and frictional behavior. To do this, we looked at how sintering temperature affected the density, porosity, Young's modulus, lattice parameters, microhardness, friction value, wear volume, and wear rate of the -Al2O3 nanostructured alloys.

2. Investigational study

2.1. Materials

One type of ceramic has been used in this work as a raw material based mainly on Al_2O_3. The latter is a union of the elements of aluminum and oxygen; its distinctive feature is that when exposed to air, it does not rust, unlike some materials. The reason for this is that it reacts with oxygen in the atmosphere. It is supplied by a ceramic company of greater than 99.99 % purity, is white in color and has particle sizes in the range of 100μ m (Fig. 1.a).

The mixtureα-Al_2O_3 is the thermodynamic stable phase of alumina, which is obtained by calcinations at high temperatures, and crystallizes, in a trigonal system. The elemental lattice also contains thirty atoms, which correspond to six molecules of alumina. The oxygen atoms are arranged in a hexagonal compact structure where the aluminum atoms occupy two thirds of the AlO_6 (octahedral) sites, as we can see in Fig. 1b. The primary lattice is plotted in a system of rhombic axes with each node, where the base contains two alumina molecules arranged in triangular diamonds arranged along the C-axis of the corresponding hexagon and the hexagonal primary cell dimensions are $a_0 = b_0 = 4.7589$ Å, co = 12.951 Å, $\alpha = \beta = 90°$ et $\gamma = 120°$ (Hezil et al., 2022).

Alumina has high mechanical strength and high temperature hardness, excellent corrosion resistance, and high chemical inertness, all of which make alumina a material that is used in a wide range of fields. Table 1 presents the main mechanical, physical, thermal, electrical and chemical properties of alumina (Hezil and Fellah, 2019).

2.2. Sample preparation

Using a high-energy ball mill)Fritsch P7), a quantity of AL_2O_3 powder was put into 80 ml cylindrical flasks. After adding 8 Agate steel balls with a diameter of 10 mm inside the container, the machine runs at a grinding speed of 450 rpm for different grinding times 0, 2, 6, 12, 18 and 24 h, followed by a cooling period of 40 min. A pressure of 100 MPa is applied to the powder using the compressor, by placing 1 g of the powder in a cylindrical mold (15 mm). The attained samples were also exposed to static pressure to gain closed absorbency and endangered to sintering at temperatures of 1450 °C in a vacuum furnace in low pressure 5×10^{-6} Pa at a constant heating rate and holding time of 15 °C/min and 19 × 103 s, correspondingly.

During which we obtained cylindrical samples of Al_2O_3 that differ in the initial size of the powder granules according to the grinding period. The following diagram illustrates the steps involved in preparing these samples (Fig. 2).

2.3. Characterization techniques

X-ray diffraction was utilized to analyze the materials' crystal arrangement utilizing a (Bruker AXS-D8) diffract meter with Cu-K radiation ($<\lambda>$ Cu = 0.15406 nm). The routine locked-coupled scanning parameters were set as follows: Voltage = 40 kV. Current = 30 mA. Goniometer angle 2θ = 15° –45°, Step size = 0.02°, Scan speed = 0.5 s/step,

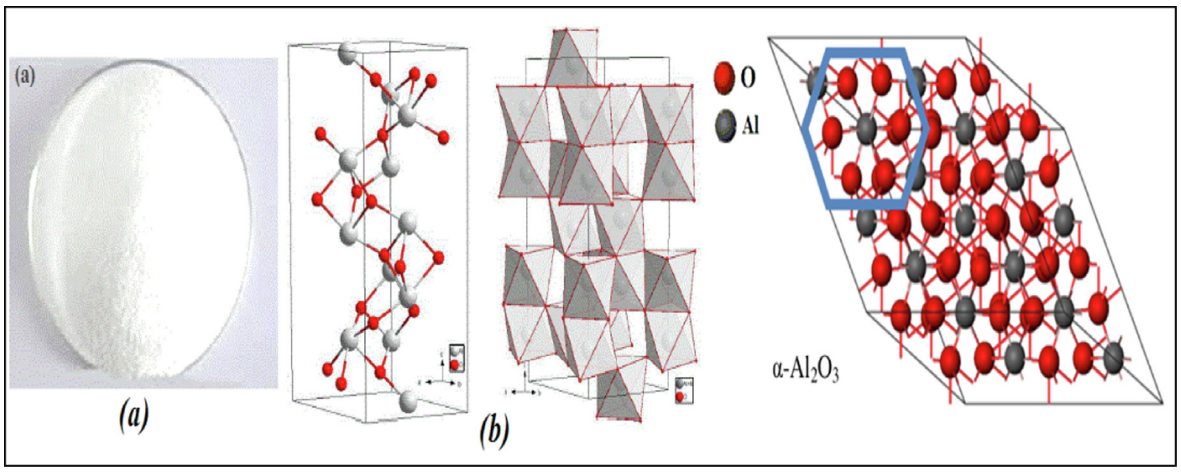

Fig. 1 (a) α-Al_2O_3nanopowder and (b) α-Al_2O_3 crystal structure.

and Divergence slit = 0.6 mm. The various sections of the materials were investigated utilizing a scanning electron microscope (JSM-6301F). The surface impurities were removed using X-ray photoelectron spectroscopy (XPS) through Al Ka irradiation by energy of 1486.6 eV. Using a Vickers diamond indenter and a force of 2 N, the Zwick ZHV2.5 hardness testing equipment was used to assess the Young's modulus and Vickers hardness. The mean of 10 measurements serves as the described charge for every illustration. The wear rate was calculated by confocal microscope (profilometer) (Wyko 9300 from Weeco).

3. Results and discussion

3.1. Microstructural Characterization

3.1.1. XRD and SEM of α-Al_2O_3Initial powder

X-ray diffraction spectrum analysis of a quantity of laboratory Al_2O_3 powder is shown in Fig. 3a. The results showed us that all the lines on the spectrum belong to the aluminum oxide with phase α and its mineral name is corundum, which corresponds to card No. 00–010-0173 (Hezil and Fellah, 2019). The peaks of α phases appearing at 25.66°, 35.23° and 37.29°, these peaks correspond to the (012), (104) and (110) planes, respectively.

Fig. 3.b shows morphology aspects of the agglomerated powders obtained from SEM of α-Al_2O_3 powder. Through the micrographs it was observed that the powders are formed by the smallest grains are not evident, giving a minimum particle size around 100 μm. The grains were comparatively angular consisting of submicron fragments which appear to have been welded together, forming larger agglomerates.

3.1.2. XRD of α-Al_2O_3 samples prepared

The latter shows that the morphological shape of the alumina powder consists of aggregates of roughly spherical and regular granules, but these aggregates contain a very large group of granules that are attached to each other. X-ray diffraction pattern analyzes of alumina samples treated at 1450 °C (Fig. 4) are performed at different times of milling (2, 6, 12, 18 and 24), where the X-ray diffraction patterns of the organized samples allow the formation of new phases in the range (2θ = 10-80°).

The diffraction spectra obtained for all samples at high temperature reveal the presence of a major crystal phase represented in α-Al_2O_3, where was observed a decrease in the strength of the peaks corresponding to this phase and the disappearance of most phases as milling time is increased. The positions of the peaks, which show strongly when beams of these rays are shed at various angles on the membrane, were determined through the study of these curves, allowing them to overlap advantageously when the Bragg condition is present. It was observed that (020), (002), and (110) are the three prominent tendencies of this phase growth and that they appear at angles of 14.21, 18.24, and 20.37 (JCPDS 96–100-0018), respectively.

After 6 and 12 h of grinding, widening of the peaks and a decrease in their intensity with increasing milling time can be observed. The disappearance of the peaks corresponding to the crystal levels (200), (2–20), (2–11), (112), (021), (311), (022), (312), (023) and (123) were also (2–32), (024), (314), (324), (6–31), (6–02) and (142) are observed. This can be attributed to reduced granule size (Arif et al., 2020).

After 18 and 24 h of grinding, almost all the peaks disappear when comparing the diffraction spectra recorded at different grinding times, with a gradual decrease in the diffraction lines of the alumina phase with increasing grinding time, this is due to the continued formation of the liquid phase as a result of its melting. The α-Al_2O_3 phase has completely melted at these two times and the X-ray diffraction pattern shows a wide band devoid of diffraction lines. This is due to the formed amorphous (glassy) phase.

The effect of grinding time at different times was also evident through the presence of a shift of the XRD peaks towards the lower angles. It should be noted that this transformation indicates the expansion and expansion of the crystal lattice, which can be explained by decreasing the ionic radius of Al^{3+} by decreasing the size of the grains and gradually converging them until they disappear and replace them with the glass phase, an increase in density, a decrease in the sample size, a decrease in the proportion of pores, stress are all factors that lead to deformation and defects in the crystal lattice.

Table 1 Some mechanical, physical, thermal, electrical and chemical properties of alumina (El-Kheshen et al., 2008; Hezil and Fellah, 2019).

Properties	Value	Symbol
Volumetric mass ($g.cm^{-3}$)Molecular weight	3.9	ρ
($g.mole^{-1}$)	102	M
Hardness (Mohs)Young's modulus	9	-
(GPa)	300–	E
Poisson's ratioBending strength	400	ν
(MPa)Clinging	0.25	σ_f
($Mpa.m^{1/2}$)	380	K_{1C}
	2–3	
Dielectric constant	9–10	ε_r
Electrical resistance at 20 °C (Ohm.cm)	$>10^{14}$	σ
Electrical insulation resistance	10–20	-
(kV/mm)		
Specific heat (J/K/kg)Heat conduction (W/m/K)	900	C_P
at 500 °CLinear dilation	10–15	λ
(10 × 6) from 20 to 1000 °C	8–9	α

3.1.3. Structural parameters

From the XRD patterns, the mesh parameter, fine stress and average grain size can be calculated. In Fig. 5a, the variance in the mean crystal size (D) and microstrains of the alpha-alumina sample is shown as a function of the sintered milling time at 1450 °C. Where a decrease in crystal size was observed accompanied by an increase in macrostrains, during which the average grain size reached 23.22 nm after it was 44.85 nm (Fig. 5a).

The d-spacing, or separation amongst crystallographic planes, serves as a strain gauge in the X Ray Diffraction method. Only crystalline, polycrystalline, and semi-crystalline materials can be used with this technique. The d-spacing changes depending on whether the material is under tension or compression; it increases when the material is in tension. The x-ray diffraction peak angular position shift caused by residual stresses in the material is directly monitored by the detector (Belassel, 2012).

The lattice factor of the α-Al_2O_3 arrangement is (a = 4.7 6 Å and c = 12.95 Å). At the temperature of 1450 °C alumina has a tendency to display higher lattice factors in line for the presence of defects and impurities, whose values were obtained from the Braggs relationship (Bouras et al., 2020):

$$n\lambda = 2dsin[03B8] \quad (1)$$

where n and λ are an integer and the wavelength of the incident wave correspondingly.

These weaknesses are announced through sample training and vary conferring to the technique and mixtures used. Among them, we mention the severe deformation of plastics and plastics during high grinding times, which leads to an increase in the intensity of dislocations and disturbances (Fig. 5b).

The literature indicates that the network parameter and particle size are directly related, indicating that as the particle size decreases, this leads to a corresponding increase in the network parameter. And this was confirmed by the experimental technique used here, where the particle size decreases with the increase of the milling time, accompanied by a continuation of the increase of the lattice parameter clearly (Zhang, 2004). The results also show that since the lattice modulus, annealing temperature range and grinding time are equivalent, the lattice parameter increases as a function of grinding time and thus defects such as ionic voids decrease. This strongly indicates that the surface tension plays a major role in determining the network parameter (Mohammed et al., 2020).

3.1.4. Grain size and distribution

Fig. 6 displays the PSD of the unmilled and milled samples at the speed of 450 rpm with milling times of 24 h. The PSD of the unmilled sample is trimodal and expected consequences from accumulation of sub-micron (100 μm) particles caused by high heats in the flame synthesis of aluminum dioxide (Fellah et al., 2019). During the first 2 h of PSD milling, the trimodal decreases to bimodal and then significantly to monomodal which is observed after 6 h. The initial drop in PSD can be credited to the deagglomeration of weakly interacting particle clusters, with the initial particle size decreasing by ~ 60 μm. With more grinding hours, the amonomodal par-

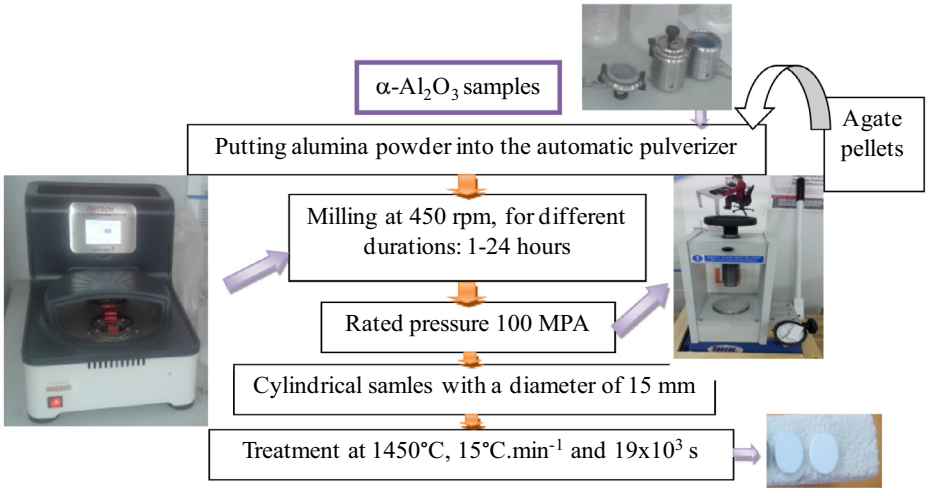

Fig. 2 The method used in the preparation of α-Al_2O_3 samples.

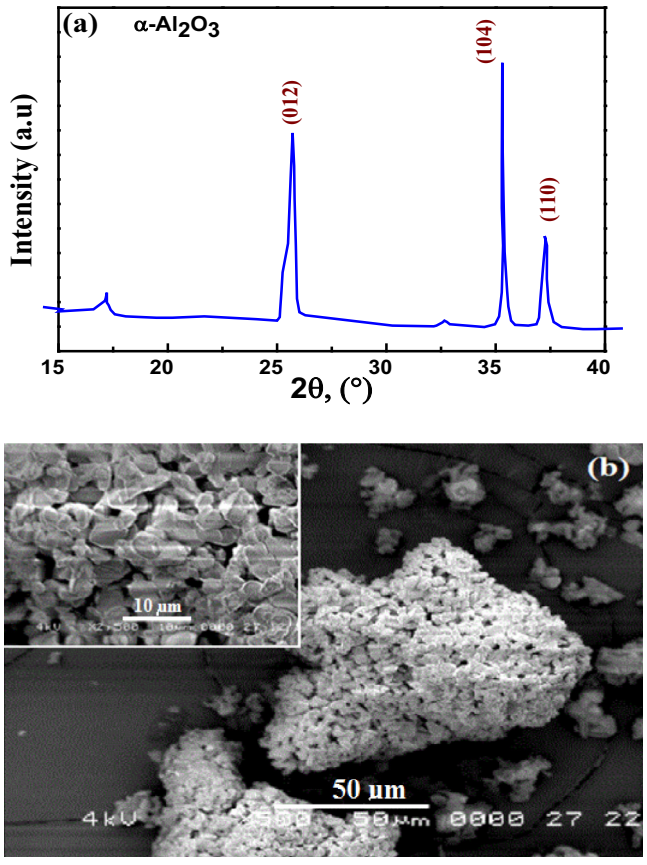

Fig. 3 The SEM morphological strating α –alumina powder.

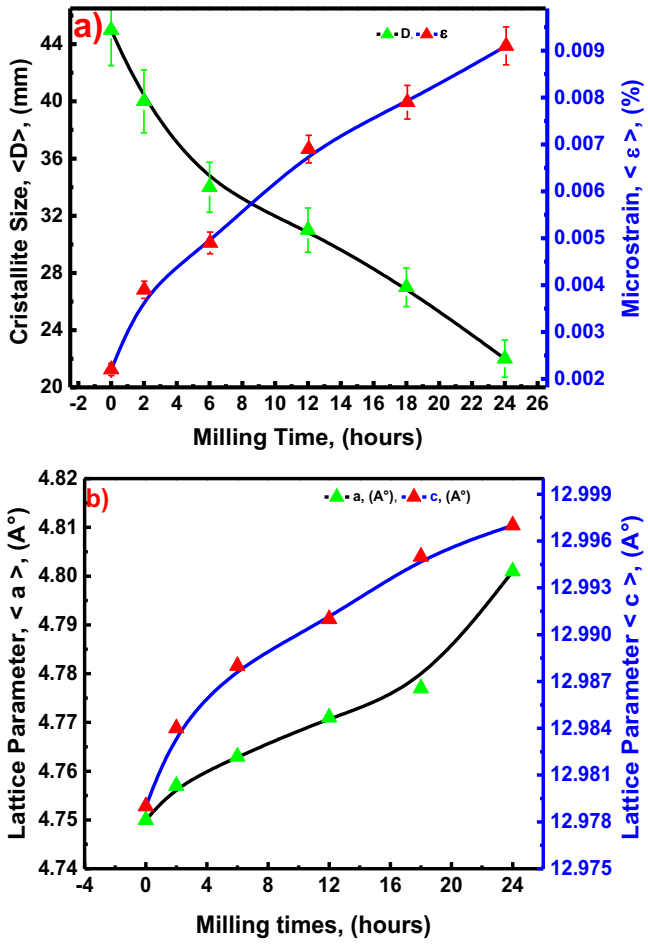

Fig. 5 Evolution of: a) mean crystallite size{D}, (nm), and microstrain {3}, (%), and b) lattice parameters{a and c}, (Å), of milled α-Al_2O_3 as function of milling times.

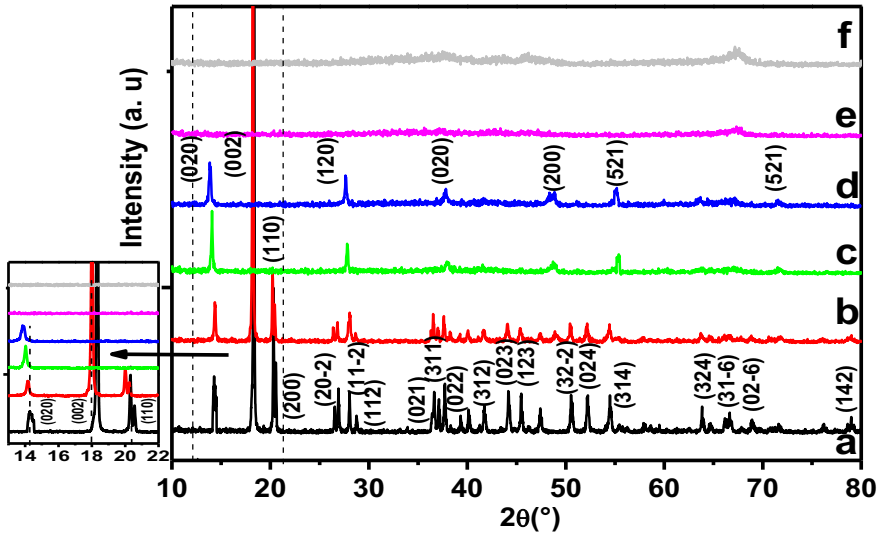

Fig. 4 X-ray diffraction of milled α-Alumina versus milling time treated at 1450 °C a): 0 h, b): 2 h, c):6h, d): 12 h, e):18 h, f): 24 h.

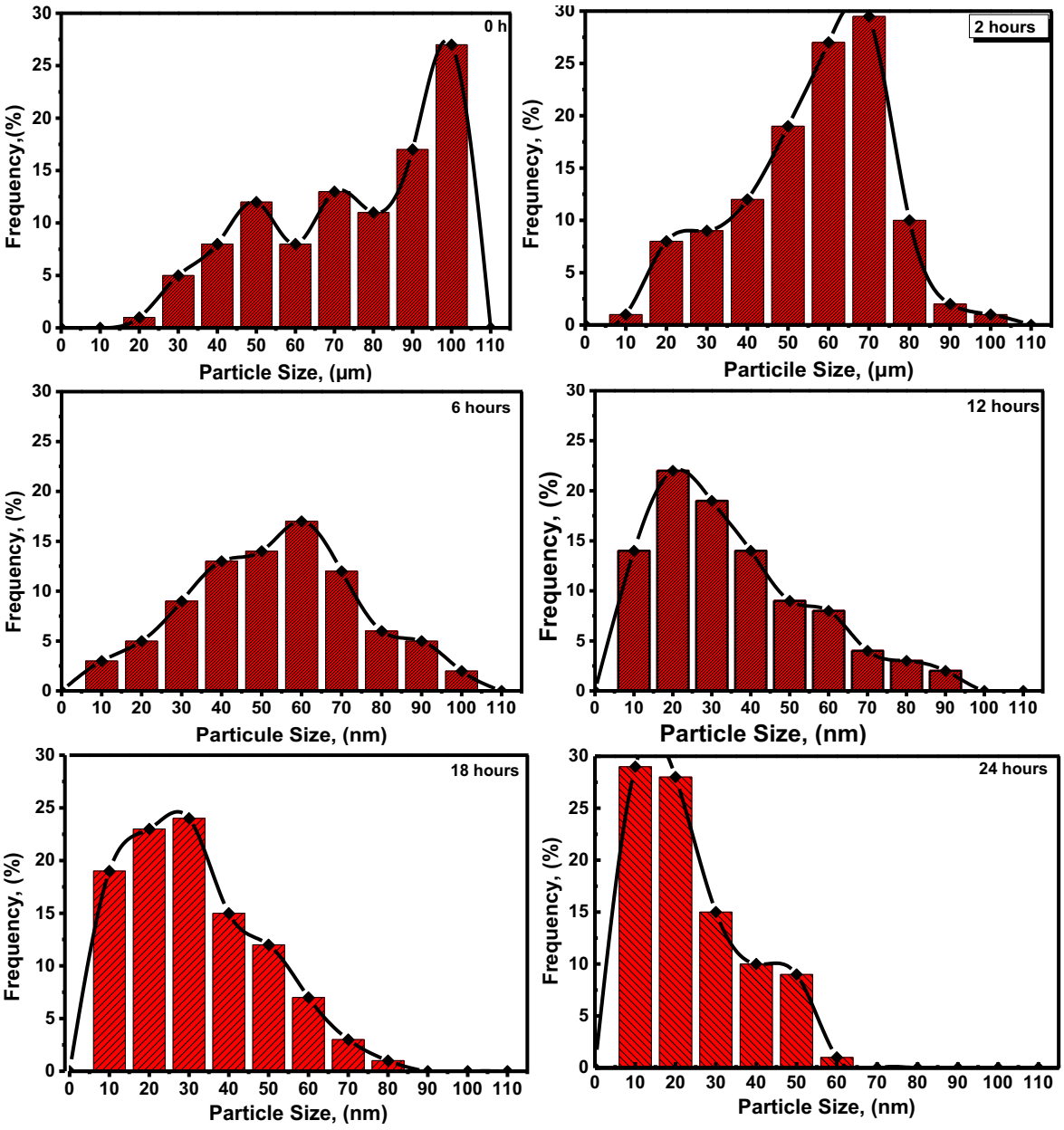

Fig. 6 Particle size distribution (PSD) graphs of milled alumina α- Al_2O_3 as function of milling times (hours).

ticle size distribution outcomes in both de-agglomeration and particle fracturing, and at 24 h the PSD particle size reaches approximately 10 nm (Thembinkosi Donald Malevu, 2015; Ramasamy et al., 2020).

3.2. Mechanical characterization

3.2.1. Porosity and relative density measurements

The mean pore size (MPS) of α-Al_2O_3 alloys at various grinding times is shown in Fig. 7.a,b. According to MPS, at 1450 °C sintering temperature, the pore size of the powders reduced and the density increased with increasing grinding time. This decrease in particle size proves that samples sintered at high temperatures reduce the proportion of pores and are more uniform. The percentage of pores reached 0.04 % within 24 h of grinding after it was approximately 0.20 %, while the density reached 96 % after the same highest grinding time.

As the calcification neck grows with rising temperature and the open pores eventually close to form closed pores during the sintering process of metal powders, these outcomes can be explained by accelerating the atom's rapid diffusion speed (Kadirgama et al., 2017).

Additionally, because of the lower particle size and higher interface energy, sintering neck formation is made easier. Thus, it may be concluded that the pore size distribution is strongly impacted by the development of a calcified neck.

The α-Al_2O_3 sample sintered at 1450 °C after 24 h of grinding displayed anactualextraordinary density of 96%, which gives it potential and efficacy in orthopaedic applications (Fellah et al., 2019).

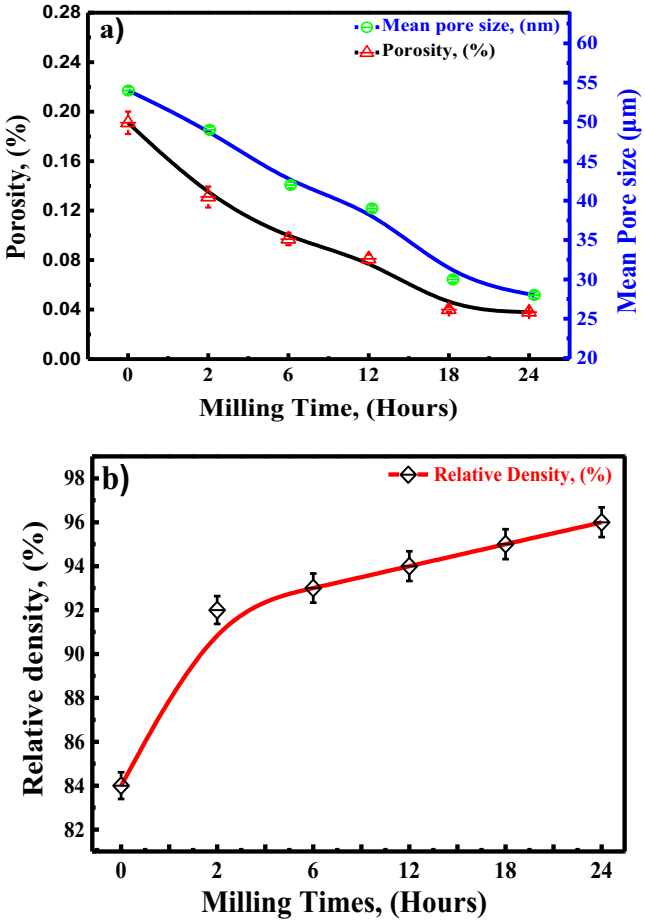

Fig. 7 Evolution of: a) Porosity frequency, (%) and mean pore size (µm) and b) the relative density, (%) of milled alumina alpha as function of milling times.

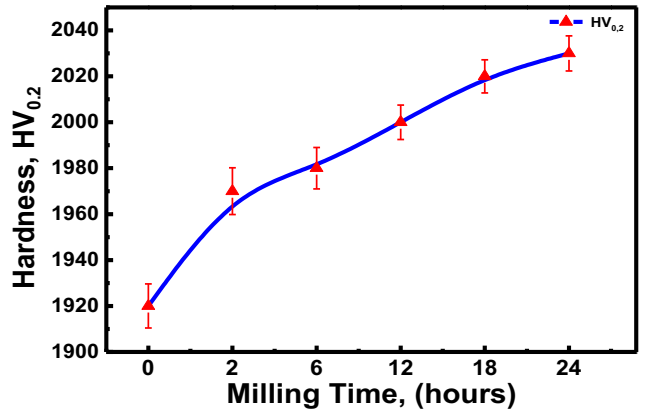

Fig. 8 Evolution of micro hardness of milled and sintered α-alumina as a function of milling times.

3.2.2. Hardness measurements

The "Zwick ZHV 2.5″ hardening test instrument was used to determine microscopic hardness for the mechanical possessions of the double pillars using the Vickers hardware examination. The test procedure entails placing ceramic sample pieces at a distance from each other, separated by diamonds

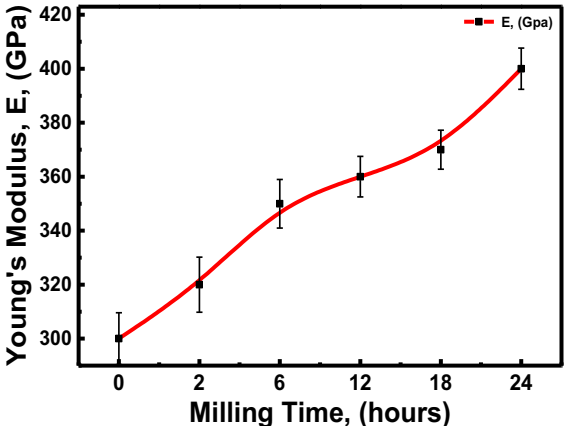

Fig. 9 Evolution of Young modulus of sintered α-alumina as a function of milling times.

in the shape of a pyramid with a square base and a 136-degree angle between the opposing faces. The area of the slope surface is measured after the indiscriminate distance. Vickers stiffness is calculated by dividing the value of the load by the square area of the height distance per millimeter. The load was applied to one sample in four different areas of the sample shells in order to compute the average area of the slope shallowafterward the indiscriminate distance (Wang et al., 2012). After annealing of the samples, Fig. 8 displays the modification in microscopic hardness in relations of grinding time change on the samples preserved at 1450 °C. The values of microscopic hardness increase with the increasing grinding time, which is extra pronounced at the time of 24 h. This is explained by the size of the particles, which decreases the more we double the crushing process, and also to the superiority of the stages resulting from the heat treatment of the compound α-Al_2O_3, which has good mechanical properties by reducing the proportion of pores. Thus, reducing the size of the nanoparticles and the sintering process and then glazing are factors contribute to the emergence of more solid crystal phases that help the cohesion of the grains and thus give a denser and more consistent microstructure (Abu-Surrah and Al-Degs, 2022; Zhang, 2004; Hezil et al., 2022; FatemehMirjalili and Abdullah, 2011).

3.2.3. Young's modulus measurements

Among the mechanical properties is also the linear modulus of elasticity (Young's modulus), which expresses the elasticity of the material and shows how the material behaves under the influence of forces and it is a linear relationship (FatemehMirjalili and Abdullah, 2011). The constants are obtained from laboratory experiments, and that was clarified in Fig. 9 from the variance with different crushing times. From the latter, we notice that the value of the modulus of elasticity increases with the increase in the grinding time.

To describe the mechanical behavior and wear resistance of the alloys, different ratios between the modulus of hardness and elasticity were used. Fig. 10 showed a behavior similar to that of hardness, as its value increases with the increase in milling time. The highest ratios of H/E and H^3/E^2 were estimated to be 0.8115 GPa and 0.63 GPa after milling time of 24 h, respectively. While their values before grinding were

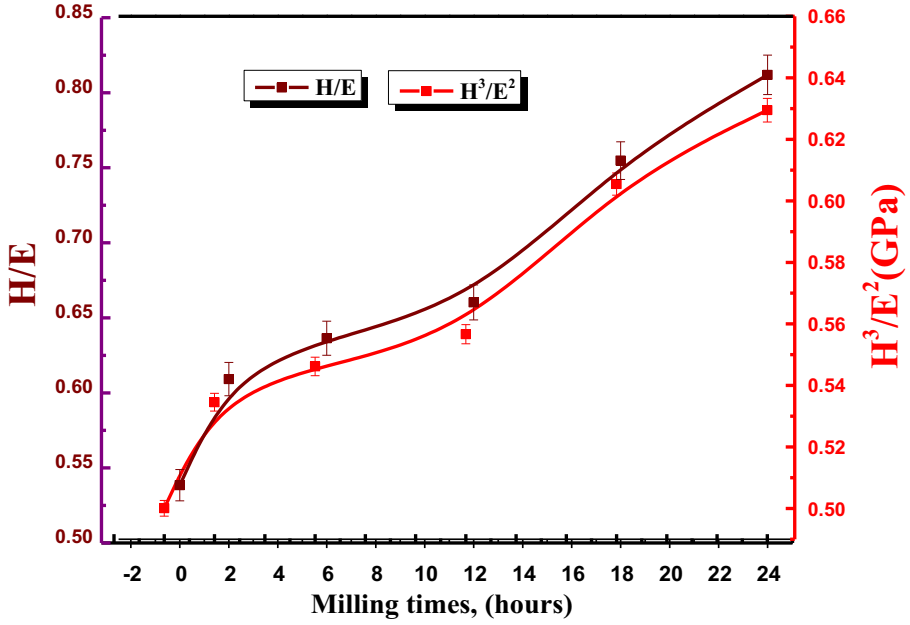

Fig. 10 H/E and H^3/E^2 ratio's of α-Al_2O_3samples as a function of milling times.

around 0.53 GPa (H/E) and 0.52 GPa (H^3/E^2). These factors lead to a high resistance to fracture and excellent elastic deformations, which are properties that promote better resistance to abrasion and thus an improvement in the mechanical properties of the samples with the largest milling time (24 h).

This can be attributed to the increase in the density by reducing the size of the alumina particles, which leads to an increase in the strength of the samples and is less prone to fracture.Also, having high flexibility means maintaining its shape regardless of the external forces applied to it and this is what is known as a rigid body, in which deformations are neglected Fig. 10.

This serves us in the medical field, because the greater the bone density, the greater the bone mass, and thus the less prone to fracture and exposure to osteoporosis, which is closely associated with the bone tissue that represents the solid

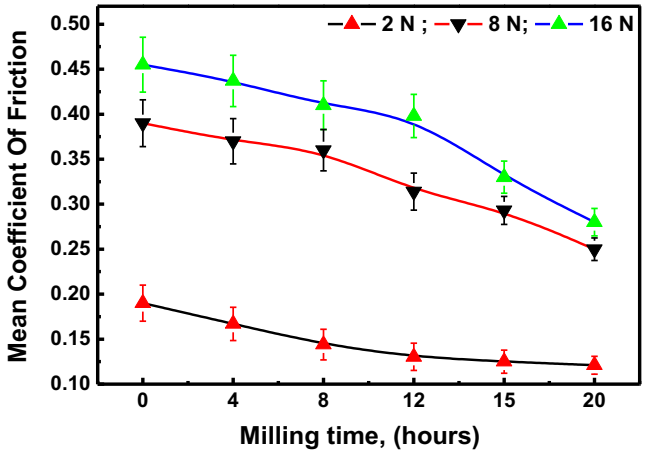

Fig. 11 Mean friction coefficiens of milled Al_2O_3-α as a function of milling times (h), under different applied load (N).

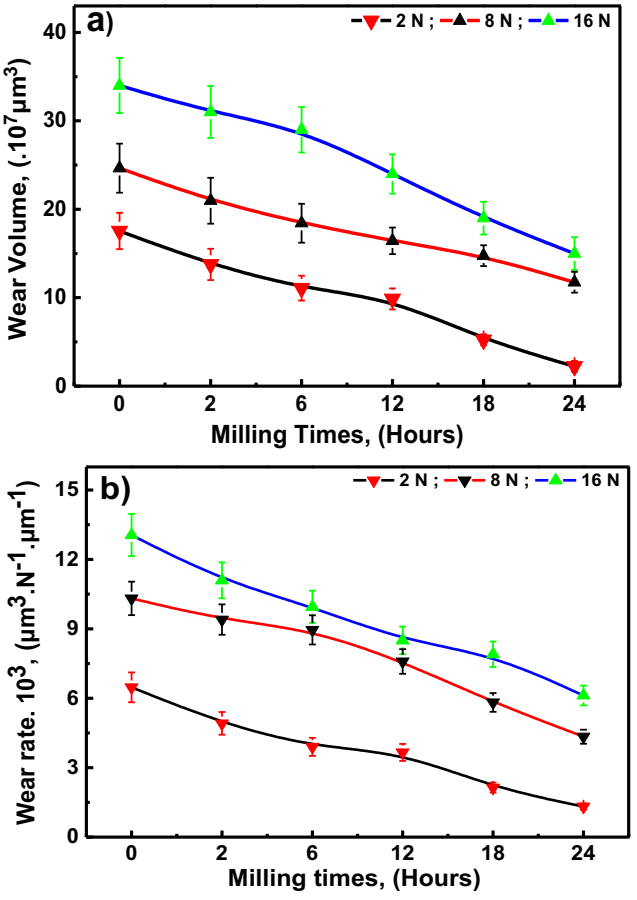

Fig. 12 Development of: (a) wear capacity (μm^3), and (b) wear rate ($\mu m^3.N^{-1}.\mu m^{-1}$) of milled Al_2O_3-α as a function of milling times (h) atdiverse applied load (N).

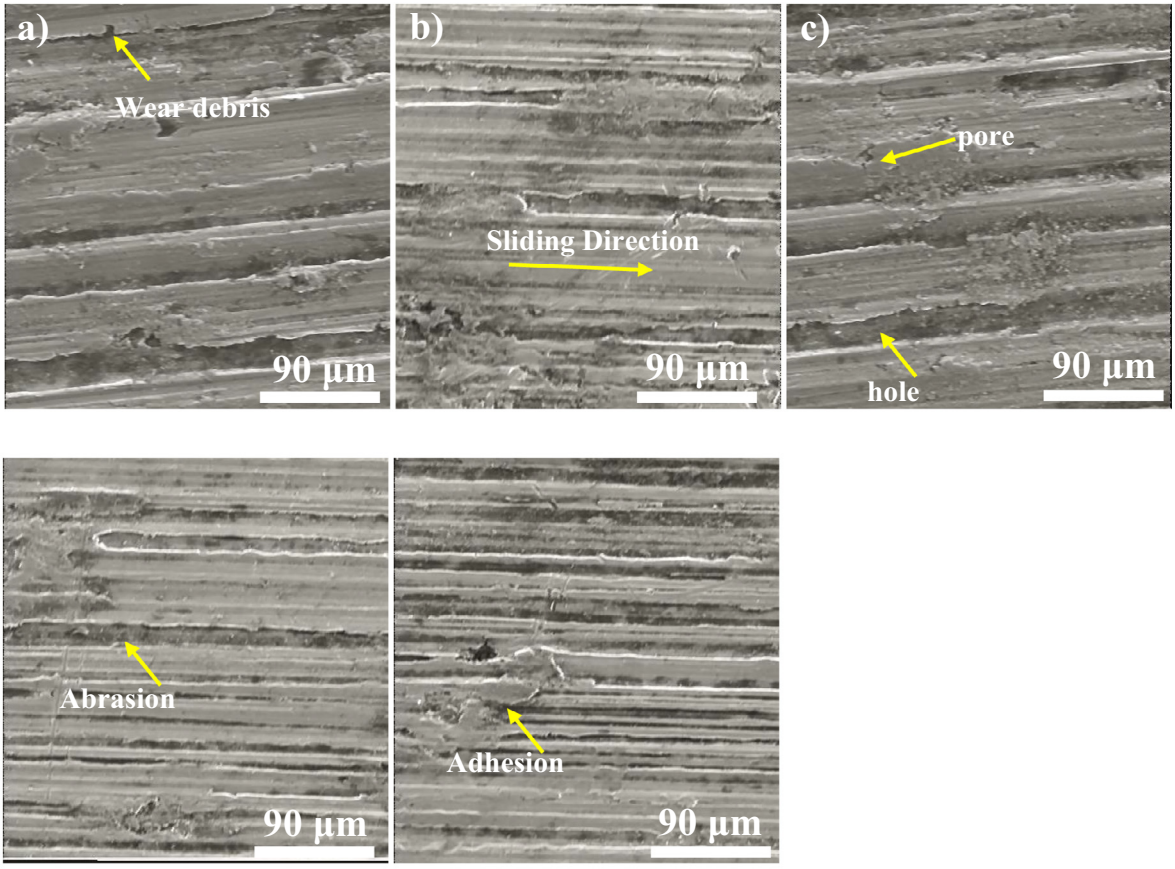

Fig. 13 SEM images showing the effect of milling time of a) 2 h, b) 6, c) 12, d) 18, e) 24 h on surface morphology of sintered and compacted alumina powders.

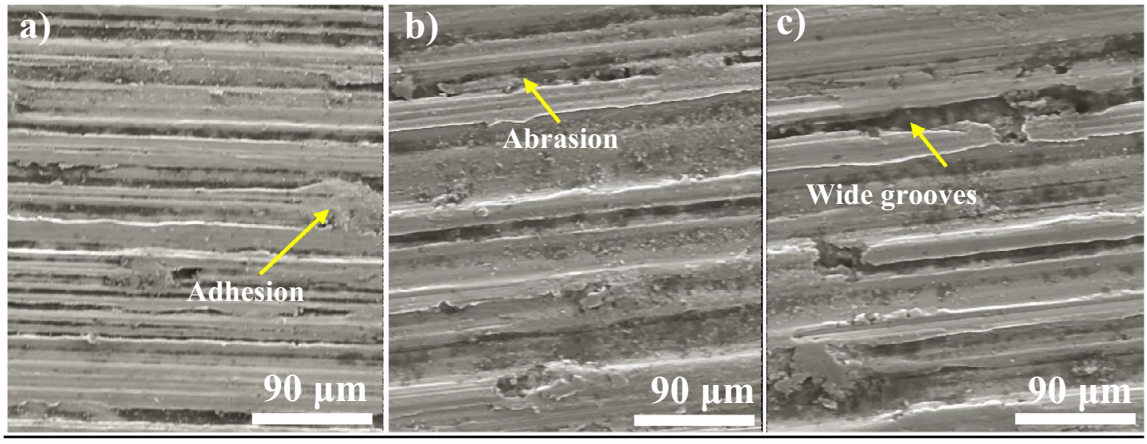

Fig. 14 SEM images showing the effect of applied loads: a)- 2 N, b)- 8 N and c) −16 Non the surface morphology of milled α-alumina sample for 24 h.

part of the bones that in turn form the internal structural support for the body of the organism Neighborhood. These factors enhance the mechanical properties of the sintered samples and thus increase the wear resistance which is accompanied by reduced surface porosity and improved tribological performance (Zhang, 2004).

3.3. Tribological description

3.3.1. Evolution of friction measurement

The sintered and compacted illustrations were refined to a shallow roughness of approximately 6 nm (Zhang, January 2004), and then tribological investigates were agreed with utilizing

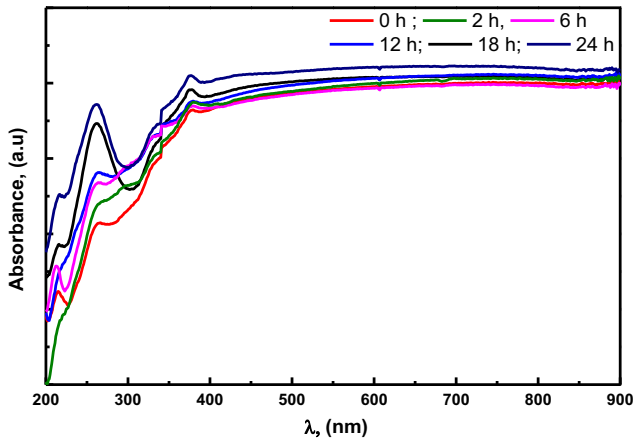

Fig. 15 UV–Vis Absorption Spectra of milled α -Al_2O_3 with different milling times (h).

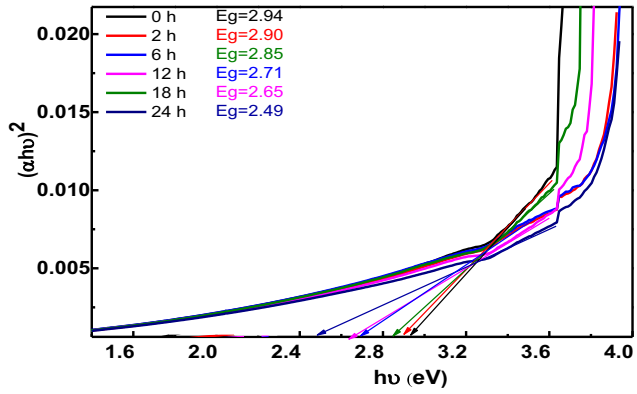

Fig. 16 Tauc plot of Milled α -Al_2O_3 with different milling times for determining the band gap.

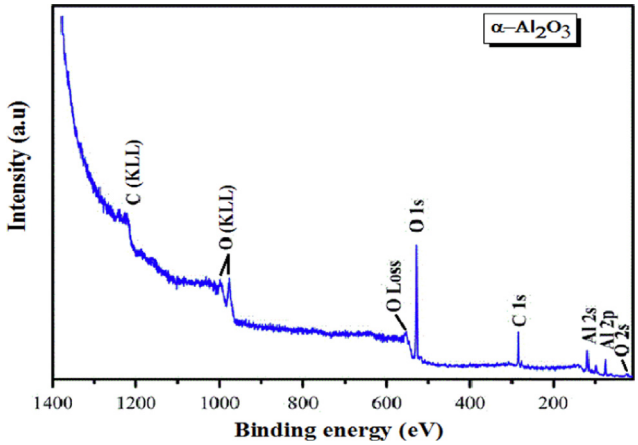

Fig. 17 Survey Scan of α-Al2O3 sample sintered at 1450 °C.

ball-on-disc formation in humid conditions and body fluid simulation using Ringer's solution with a constant linear velocity of 10 mm.s^{-1} at various normal loads of 2, 8, and 16 N, correspondingly. Using alumina (Al_2O_3) balls of 6 mm in diameter with a sliding distance of 200 m, the wear rate was designed as anoccupation of the damaged volume and the milling time measured by an interference confocal microscope.

Depending on the mechanical properties in Fig. 11, it is noted that the coefficient of friction decreases with increasing grinding time, while its value increases with the increase in the applied compressive force. Tests showed that there are fluctuations in the development of the coefficient of friction, as after 20 h the coefficient of friction reached 0.12 after it was 0.19 under an applied pressure of 2 N. In the same period, after applying pressure of 8 and 16 N, the coefficient of friction increased to 0.25 and 0.28, respectively. This is attributed to the effect of thermal softening / stress on the alumina samples. It can also be explained by the separation of surface materials that are annealed under high pressure, which leads to increased corrosion. Thus, it can be said that the main factor to reduce friction is the increase in grinding time, regardless of the value of the applied load (Musil et al., 2002; Oliver and Pharr, 1992).

3.3.2. Evolution of volume and wear rate

To confirm the previous results, measurements of the erosion volumes were carried out by means of two-dimensional scans of the erosion paths using optical measurement. Fig. (12.a and b) shows the evolution of the corrosion rate and wear size of the α -Al_2O_3 samples sintered at 1450 °C with different grinding times. The same behavior was observed for both the volumes and rate of wear, as the alloys decrease with increasing grinding time (0–24 h) while they increase with increasing load (2, 8 and 16 N). The results showed that the Al_2O_3 alloy applied to it with a load of 2 N and milled for 24 h had a minimum value of 1.94 μm^3 wear volumes (Fig. 12.a) and a wear rate of 1.33 ($\mu m^3.N^{-1}.\mu m^{-1}$) (Fig. 12.b) after they were 17.70 μm^3 and 6.47 ($\mu m^3.N^{-1}.\mu m^{-1}$), respectively. To confirm and know the effect of the force applied on the surface of the best sample obtained during grinding for 24 h, it was analyzed with the help of SEM analysis, where the images (Figs. 13 and 14) show that the greater the applied force (2, 4 and 6 N), the more fragile the surface becomes and more susceptible to debris. This gave a more deformed surface, which resulted in the emergence of cracks with depth and the increase in the impact of corrosion and debris and its spread along the surface of the sample (Zhang, 2004). The milling time used in this work resulted in a reduced grain size, which in turn allowed enhancing its mechanical properties. These features enable it to be effective in reducing the release of metal ions and reduce the formation of debris without having a negative role in the body, thus making it suitable and important in the field of biomaterials.

3.3.3. SEM morphology of α-Al_2O_3 samples

The microstructure is important in knowing the mechanism, by which the sintering process was carried out for different milling times, as well as the corrosion mechanism of the surface and how the effects of slips are distributed on it. As shown in Fig. 13. The five-studied milling times applied to 200 m of slip showed a difference in the result, where significant damage was observed in the samples that were milled at 2, 6 and 12 h with the formation of cracks on the corrosion path spaced apart due to the wide formation of slip bars.

There is also a depth (in length and width) caused by slipping, which caused a large deformation in the surface of the samples and the appearance of pores in a disparate way along the sample, which could be attributed to the presence of interstitial voids that permeate the grains, which greatly con-

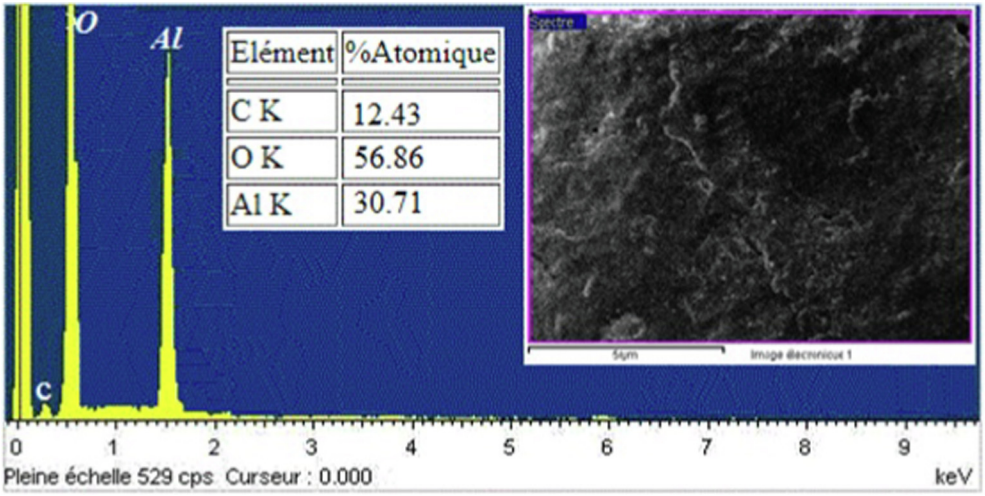

Fig. 18 EDS spectrum of α-Al_2O_3 sample sintered at 1450 °C.

tributed to the expansion of the erosion towards the depth (Fellah et al., 2017).

This decreased significantly with the increase of the milling time for both samples, 18 and 24 h, in the presence of the slip lines very close to each other and the absence of drilling depth, to form the wear-resistant glass phase, which is highly resistant to mechanical attack and more solid, and this was confirmed previously by the coefficient of friction (Zhang, 2004). The images also show the presence of minute debris left over the cracks resulting from the erosion process.

3.4. Optical analysis

All alumina alloys made with various milling times were investigated for absorption studies in the wavelength range (200—900 nm) (0, 2, 6, 8, 12, 18 and 24 h). Fig. 15, which depicts the absorbance relationship as a function of wavelength, demonstrates that for all doped alloys, the absorbance rises as the wavelength increases.

Its values show that it is the lowest possible in a region, and the absorbance principles create to increase progressively with increasing wavelength values in the infrared district of the spectrum within the range 200–400 nm and the visible region 400–700 nm, after which its value almost stabilizes in the 700-infrared region −900 nm. Alumina has a very weak absorption, but it increases with increasing milling times, since there is an upsurge in the captivation of observable light energy, which resembles to an intensification in the number of electronic transitions between the transmission band and the valence band.

To identify the energy gap values of the samples, it was calculated using Tauc's equation, which is presented in Fig. 16. The organized samples are utilized the next association (Musil et al., 2002; Oliver and Pharr, 1992; Dammak et al., 2012; Fellah et al., 2019; Bouras et al., 2023; Fellah et al., 2014):

$$\alpha \mathbf{h}\nu = \mathbf{A} \cdot \left(\mathbf{h}\nu - \mathbf{E_g}\right)^{1/2} \quad (2)$$

With A: constant, E_g: optical gap, hν: photon energy.

The plot provides a non-straight line in the photon energy band, indicating that the alumina samples have an indirect electronic transmission with a bandgap of 2.94 eV, 2.90 eV, 2.85 eV, 2.71 eV, 2.65 eV and 2.49 eV that corresponds to a milling time of 0, 2, 6, 12, 18 and 24 h, respectively.

This suggests that the visible wavelengths can be absorbed by the white alumina combination. As a result, it can be suggested as a photocatalyst when exposed to visible light.

3.5. X-ray photoelectron spectroscopy (XPS)

In order to inspect elements extant and their chemical formal in the as synthesized α-Al_2O_3 sample, the X-ray photoelectron spectroscopy (XPS) measurement was carried out. Fig. 17 from the survey scan shows that, other from C-1 s signals, there are no impurity elements on the sample's surface. These signals (C 1 s) were expected as synthesis was carried out in an open environment and the model was also uncovered to air before the measurements. Analysis showed that the high determination core level scans for O-1 s and Al-2 s.

The chemical compositions of α-Al2O3 confirmed by EDS spectra and shown in Fig. 17 with reference peak at 0 Kev and the results obtained by XPS spectra were confirmed. Spectrum study reveals the presence of aluminium and oxygen elements with 30.71%, 56.86% and 12.43% atomic weight percentages without impurities and shows that only Al, O and C are present in the sample corresponding to their binding energies (see Fig. 18.).

4. Conclusions

Alumina alloys are required for many biomedical applications and the most common among them is α-Al_2O_3. In this study, samples were fabricated using different milling times by high-energy mechanical grinding. X-ray diffraction and scanning electron microscopy showed the crystal structure with determination of the phases and surface morphology of samples prepared with different milling times 2, 6, 12, 18 and 24 h.

To describe the generated samples and determine the impact of grinding time on the structural and mechanical properties, hardness tests were carried out. It was perceived that samples sintered at 1450 °C and milled for 24 h had the smallest crystalline size and pores, with increased comparative concentration and automated possessions. Tribological examinations were carried out at variable normal masses

to describe the wear and friction behavior and exposed that the sample with the same previous behavior obtainable the final friction coefficient and wear frequency.

Availability of data and materials

All data generated or analysed during this study are included in this published article.

Declaration of Competing Interest

The authors declare that they have no known competing financial interests or personal relationships that could have appeared to influence the work reported in this paper.

References

Abu-Surrah, A., Al-Degs, Y., 2022. Utilization of nanosize spent oil shale for water treatment: application of top-down nanonization technology for solid residues. Environ. Sci. Pollut. Res. 29, 78314–78329. https://doi.org/10.1007/s11356-022-21356-x.

Anjaneyulu, U., Zhang, V., Ren, P.-G., 2019. Bioinert Ceramics for Biomedical Applications. Publisher: Biomedical Sci and Tech Series, Wiley/Scrivene.

Arif, S., Jamil, B., Bilal, M., Shaikh, N., Aziz, T., Ansari, A.H., Khan, M., 2020. Characterization of surface morphology, wear performance and modelling of graphite reinforced aluminium hybrid composites. Eng Sci Technol Int J 23, (3) 674e90.

Mohammed Belassel, 2012. Residual Stress Measurement using X-Ray Diffraction Techniques, Guidelines and Normative Standards, SAE Int. J. Mater. Manf. 5(2). doi:10.4271/2012-01-0186.

Bhaskar, B., Nagarjuna, V. 2021. Biomaterials, Tissue Engineering, and Regenerative Medicine: A Brief Outline. In Biomaterials in Tissue Engineering and Regenerative Medicine; Springer: Singapore, pp. 3–17.

Bouras, D., Mecif, A., Barille, R., Harabi, A., Rasheed, M., Mahdjoub, A., et al, 2018. Cu:ZnO deposited on porous ceramic substrates by a simple thermal method for photocatalytic application. Ceram. Int. 44 (17), 21546–21555.

Bouras, D., Mecif, A., Barille, R., Harabi, A., Zaabat, M., 2020. Porosity properties of porous ceramic substrates added with zinc and magnesium material. Ceram. Int. 46, 20838–20846.

Bouras, D., Mecif, A., Harabi, A., Barillé, R., Mahdjoub, A.H., Zaabat, M., 2021. Economic and ultrafast photocatalytic degradation of orange II using ceramic powders. Catalysts 11 (733).

Bouras, D., Fellah, M., Mecif, A., Barillé, R., Obrosov, A., Rasheed, M., 2023. High photocatalytic capacity of porous ceramic–based powder doped with MgO. J. Korean Ceram. Soc. 60, 155–168.

Shifeng Dai,James C. Hower,Robert B. Finkelman,Ian T. Graham, David French,Colin R. Ward,Greta Eskenazy,QiangWei,Lei Zhao, Organic associations of non-mineral elements in coal: A review, International Journal of Coal GeologyVolume 218, 1 February 2020, 103347. https://doi.org/10.1016/j.coal.2019.103347.

Dammak, M., Kharrat, M., Smaoui, I., Rhaiem, S., 2012. Effects of the test conditions on the friction and wear of polyethylene. Int. J. Microstructure and Materials Properties 7 (5), 400–416.

El-Kheshen, A.A., Khaliafa, F.A., Saad, E.A., -Kheshen et al., September 2008. Rania Elwan, Effect of Al2O3 addition on bioactivity, thermal and mechanical properties of some bioactive glasses. Ceram. Int. 34 (7), 1667–1673. https://doi.org/10.1016/j.ceramint.2007.05.016.

FatemehMirjalili, Luqman Chuah Abdullah, HasmalizaMohamad, A. Fakhru'l-Razi, A. B. Dayang Radiah, R. Aghababazadeh, Process for Producing Nano-Alpha-Alumina Powder, International Scholarly Research Network, ISRN Nanotechnology, Volume 2011, Article ID 692594, 5 pages. doi:10.5402/2011/692594.

Fellah, M., Labaïz, M., Assala, O., Dekhil, L., Taleb, A., Rezag, H., Iost, A., 2014. Tribological behavior of Ti-6Al-4V and Ti-6Al-7Nb Alloys for Total Hip Prosthesis. Adv. Tribol. 2014. https://doi.org/10.1155/2014/451387.

Fellah, M., Linda, A., Abdul Samad, M., Montagne, A., 2017. Effect of replacing vanadium by nobium and iron on the tribological behavior of HIPed titanium alloys. Acta Metallurgica Sinica. (English. Letter.) 30 (11), 1089–1099.

Fellah, M., Hezil, N., Hussein, M.A., Abdul Samad, M., Touhami, M. Z., Montagne, A., Iost, A., Obrosov, A., Weiss, S., 2019. Preliminary investigation on the bio-tribocorrosion behaviour of porous nanostructured β-type titanium based biomedical alloy. Materials Lettres 257, 126755.

Fellah, M., Hezil, N., Abdul Samad, M., Touhami, M.Z., Montagne, A., Iost, A., Mejias, A., Kossman, S., 2019. The Effect of Milling Time on Structural, Friction and Wear Behavior of Hot Isostatically Pressed Ti–Ni Alloys for Orthopedic Applications. Miner. Met. Mater. Ser., 865–875

Fellah, M., Hezil, N., Leila, D., Abdul Samad, M., Djellabi, R., Kosman, S., Montagne, A., Iost, A., Obrosov, A., Weiss, A., 2019. Effect of sintering temperature on structure and tribological properties of nanostructured Ti−15Mo alloy for biomedical applications. Trans. Nonferrous Met. Soc. China 29 (11), 2310–2320. https://doi.org/10.1016/S1003-6326(19)65137-X.

Fellah, M., Hezil, N., Abdulsamad, M., Djellabi, R., Montagne, A., Mejias, A., Kossman, S., Iost, A., Purnama, A., Obrosov, A., Weiss, S., 2019. effect of molybdenum content on structural, mechanical, and tribological properties of hot isostatically pressed b-type titanium alloys for orthopedic applications. Journal Of Materials Engineering And Performance 28 (10), 5988–5999.

Fellah, M., Hezil, N., Touhami, M.Z., Obrosov, A., Weiß, S., Egor, B. K., Andrey, M., 2019. Lider, Montagne A, Iost A, Enhanced Structural and Tribological Performance of Nanostructured Ti–15Nb Alloy for Biomedical Applications. Results Phys. 15,. https://doi.org/10.1016/j.rinp.2019.102767 102767.

Fellah, M., Naouel, N., Touhami, M.Z., Abdul Samad, M., Obrosov, A., Bokov, D.O., Marchenko, E., Montagne, A., Iost, A., Alhussein, A., 2020. Structural, Tribological and Antibacterial Properties of (α + β) based Ti-Alloys for Biomedical Applications, j. Mater. Res. technol. 9 (x x), 14061–14074.

X. Gallart, J. Riba, J.A. Fernández-Valencia, G. Bori, E. Muñoz-Mahamud, A. Combalia, Hip prostheses in young adults. Surface prostheses and short-stem prostheses, Vol. 62. Issue 2. pages 142-152 (March - April 2018, DOI: 10.1016/j.recote.2018.01.003.

Ghasemi-Mobarakeh, L., Kolahreez, D., Ramakrishna, S., Williams, D., 2019. Key terminology in biomaterials and biocompatibility. Curr. Opin. Biomed. Eng. 10, 45–50.

González-Masís, J., Cubero-Sesin, J.M., Campos-Quirós, A., Edalati, K., 2021. Synthesis of biocompatible high-entropy alloy TiNbZr-TaHf by high-pressure torsion. Mater. Sci. Eng. A 825, 141869.

Granchi, D., 2017. Lucia Maria Savarino, Gabriela Ciapetti, Nicola Baldini, Biological effects of metal degradation in hip arthroplasties. Crit. Rev. Toxicol. 48 (2), 1–24. https://doi.org/10.1080/10408444.2017.1392927.

Hamisah Ismail, M. Hasmaliza, materials Bioactivity and Biocompatibility Properties of Sustainable Wollastonite Bioceramics from Rice Husk Ash/Rice Straw Ash: A Review, Materials 14(18), 5193 (18), 2021:1-27 DOI: 10.3390/ma14185193.

Hezil, N., Aissani, L., Fellah, M., Abdul Samad, M., Obrosov, O., 2022. Chekalkin Timofei, Ekaterina Marchenko, Structural, and Tribological Properties of Nanostructured α + β Type Titanium Alloys for Total Hip, j. Mater. Res. technol. 19, 3568–35780.

Hezil, N., Fellah, M., 2019. Synthesis, structural and mechanicalproperties of nanobioceramic (α-Al2O3). J. Aust. Cera. Soc 55 (4), 1167.

Jalili, P., Huet, S., Lanceleur, R., Jarry, G., Hegarat, L.L., Nesslany, F., Hogeveen, K., Fessard, V., 2020. Genotoxicity of aluminum and aluminum oxide nanomaterials in rats following oral exposure. Nanomaterials 10, 305.

Jing, G.-W., Xie, Q., Tong, J., Liu, L.-Z., Jiang, X., Si, L., April 2022. Early Intervention of Perioperative Delirium in Older Patients (>60 years) with Hip Fracture: A Randomized Controlled Study. Orthop. Surg. 14 (32). https://doi.org/10.1111/os.13244. License CC BY-NC-ND 4.0.

José Hafid Roque-Ruiz,Nahúm A.Medellín-Castillo,Simón YobannyReyes-López,Fabrication of α-alumina fibers by sol-gel and electrospinning of aluminum nitrate precursor solutions, Results in Physics. Volume 12, March 2019, Pages 193-204. https://doi.org/10.1016/j.rinp.2018.11.068.

Kadirgama, K., Ramasamy, D., El-Hossein, K.A., Hwa, K.C., Kadirgama, G., 2017. Assessment of Alternative methods of preparing internal combustion engine cylinder bore surfaces for frictional improvement. J. Braz. Soc. Mech. Sci. Eng. 1–15.

Kim, Y.-S., Chung, Y.-H., Seo, D.-S., Choi, H.-S., Lim, C.-H., 2018. Twenty-eight-day repeated inhalation toxicity study of aluminum oxide nanoparticles in male Sprague-Dawley rats. Toxicol. Res. 34, 343–354.

Krause, B.C., Kriegel, F.L., Rosenkranz, D., Dreiack, N., Tentschert, J., Jungnickel, H., Jalili, P., Fessard, V., Laux, P., Luch, A., 2020. Aluminum and aluminum oxide nanomaterials uptake after oral exposure-a comparative study. Sci. Rep. 10, 2698.

Li, X., Haonan, X.u., Wang, Q.i., Li, S., Xiao, H., Zhang, L.i., 2019. MingTang, Lifu Chen, Control of continuous α-A_l2_O3 fibers by self-seeding and Si_O2-Sol doping. Ceram. Int. 45 (9), 12053–12059. https://doi.org/10.1016/j.ceramint.2019.03.101.

Li, H., Wang, P., Wen, C., 2022. Recent Progress on Nanocrystalline Metallic Materials for Biomedical Applications. Nanomaterials 12 (12), 2111. https://doi.org/10.3390/nano12122111.

Marin, E., Boschetto, F., Pezzotti, G., 2020. Biomaterials and biocompatibility: An historical overview. J. Biomed. Mater. Res. Part A 108, 1617–1633.

Mechanical properties of bioactive glasses, ceramics, glass-ceramics and composites: State-of-the-art review and future challenges. Mater. Sci. Eng. C. 2019;104:109895. doi: 10.1016/j.msec.2019.109895.

Mohammed, A.A., Khodair, Z.T., Khadom, A.A., October 2020. Preparation and investigation of the structural properties of α-Al_2O_3 nanoparticles using the sol-gel method. Chem. Data Collect. 29,. https://doi.org/10.1016/j.cdc.2020.100531 100531.

Musil, J., Kunc, F., Zeman, H., Poláková, H., 2002. Relationships between hardness, Young's modulus and elastic recovery in hard nanocomposite coatings. Surf. Coat. Technol. 154, 304–313. https://doi.org/10.1016/S0257-8972(01)01714-5.

Nina Zamosteanu Filip, Iulian Radu, Bogdan Veliceasa, Filip Cristiana, Biomaterials in Orthopedic Devices: Current Issues and Future Perspectives, Coatings 12(10):1544 (2022). DOI:10.3390/coatings12101544.

Oliver, W.C., Pharr, G.M., 1992. An improved technique for determining hardness and elasticmodulus using load and displacement sensing indentation experiments. J. Mater. Res. 7, 1564–1583. https://doi.org/10.1557/JMR.1992.1564.

Pietrzyk, B., Kucharski, D., Kołodziejczyk, Ł., Miszczak, S., Fijalkowski, M., 2020 Feb. Comparison of Mechanical and Barrier Properties of $Al_2O_3/TiO_2/ZrO_2$ Layers in Oxide-Hydroxyapatite Sandwich Composite Coatings Deposited by Sol-Gel Method on Ti6Al7Nb Alloy. Materials (Basel) 13 (3), 502. https://doi.org/10.3390/ma13030502. Published online 2020 Jan 21.

Ramakrishna, S., Mayer, J., Wintermantel, E., Leong, K.W., 2001. Biomedical applications of polymer-composite materials: A review. Compos. Sci. Technol. 61, 1189–1224.

Ramasamy, D., Mohanesen, K., Maria, R., Samykano, M., Kadirgama, K., Rahman, M.M., 2020. Analysis of alumina particles size and shape formation from developed planetary ball mill, iop Conf. Series. Mater. Sci. Eng. 736,. https://doi.org/10.1088/1757-899X/736/5/052032 052032.

M. A. Rodriguez Olguin, H. Atia, M. Bosco, A. Aguirre, R. Eckelt, E. D. Asuquo, M. Vandichel, J.G.E. Gardeniers, A. Susarrey-Arce, Al_2O_3 nanofibers prepared from aluminum Di(sec-butoxide)acetoacetic ester chelate exhibits high surface area and acidity, Journal of Catalysis. Volume 405, January 2022, Pages 520-533. https://doi.org/10.1016/j.jcat.2021.11.019.

Rolfson, O., Donahue, G.S., Hallsten, M., Garellick, G., Kärrholm, J., Nemes, S., 2016. Patient-reported outcomes in cemented and uncemented total hip replacements. Hip Int. 26, 451–457. https://doi.org/10.5301/hipint.5000371.

Roualdes, O., Duclos, M.E., Gutknecht, D., Frappart, L., Chevalier, J., Hartmann, D.J., 2010. In vitro and in vivo evaluation of an alumina–zirconia composite for arthroplasty applications. Biomaterials 31 (8), 2043–2054. https://doi.org/10.1016/j.biomaterials.2009.11.107.

Priya Singh, Xiaojun Yu, Alok Kumar, Ashutosh Kumar Dubey, Recent advances in silicate-based crystalline bioceramics for orthopedic applications: a review, Journal of Materials Science 57 (10), 2022. DOI: 10.1007/s10853-022-07444-w.

Suárez, J.V., Farak, J., García, M.P., Perez, J.M.R., Poisoning by metals used in prothetic materials in orthopedics and its current management,, 2021. Revista Cubana de Ortopedia y Traumatologia 35(2). License CC BY-NC 4.

Tang, X., Yuxi, Y.u., 2015. Electrospinning preparation and characterization of alumina nanofibers with high aspect ratio. Ceram. Int. 41 (8), 9232–9238. https://doi.org/10.1016/j.ceramint.2015.04.157.

Thembinkosi Donald Malevu, 2015. Thembinkosi Donald Malevu, Richard Ocaya, Effect of Annealing Temperature on Structural, Morphology and Optical Properties of ZnO Nano-Needles Prepared by Zinc-Air Cell System Method. Int. J. Electrochem. Sci. 10 (2015), 1752–1761.

Himanshu Tripathi, Sumit Kumar Hira, Sampath Kumar Arepalli, Uttam Gupta, Partha Pratim Manna, S.P. Singh, Structural Characterization and in Vitro Bioactivity Assessment of SiO2-CaO-P2O5-K2O-Al2O3 Glass as Bioactive Ceramic Material, June 2015, Ceramics International 41(9). DOI: 10.1016/j.ceramint.2015.05.143.

Valiev, R.Z., Prokofiev, E.A., Kazarinov, N.A., Raab, G.I., Minasov, T.B., Stráský, J., 2020. Developing Nanostructured Ti Alloys for Innovative Implantable Medical Devices. Materials 13, 967.

Senthil KUMAR Venkatraman, Rajan Choudhary, Naveensubramaniam .V, Genasan Krishnamurithy, Hanumantha Rao Balaji Raghavendran, Malliga Raman Murali, Tunku Kamarul, Anushree Suresh, Jayanthi Abraham, Sasikumar Swamiappan, Investigation on bioactivity, mechanical stability, bactericidal activity and in-vitro biocompatibility of magnesium silicates for bone tissue engineering applications, January 2022 Journal of Materials Research 37(2). DOI: 10.1557/s43578-021-00450-9.

Wang, W., Blawert, C., Zan, R., Sun, Y., Peng, H., Ni, J., Han, P., Suo, T., Song, Y., Zhang, S., et al, 2021. A novel lean alloy of biodegradable Mg–2Zn with nanograins. Bioact. Mater. 6, 4333–4341.

Wang, C.T., Gao, N., Gee, M.G., Wood, R.J.K., Langdon, T.G., 2012. Effect ofgrain size on the micro-tribological behavior of pure titaniumprocessed by high-pressure torsion. Wear 280, 28–35.

Zhang, D., 2004. Processing of Advanced Materials Using High-Energy Mechanical Milling. Prog. Mater Sci. 49 (3–4), 537–560. https://doi.org/10.1016/S0079-6425(03)00034-3.